



### **Science Arts & Métiers (SAM)**

is an open access repository that collects the work of Arts et Métiers Institute of Technology researchers and makes it freely available over the web where possible.

This is an author-deposited version published in: <https://sam.ensam.eu>  
Handle ID: <http://hdl.handle.net/10985/7420>

#### **To cite this version :**

Paul SANDULESCU, Fabien MEINGUET, Antoine BRUYERE, Eric SEMAIL, Xavier KESTELYN - Control Strategies for Open-End Winding Drives Operating in the Flux-Weakening Region - IEEE Transactions on Power Electronics - Vol. 29, n°9, p.4829- 4842 - 2014

Any correspondence concerning this service should be sent to the repository

Administrator : [scienceouverte@ensam.eu](mailto:scienceouverte@ensam.eu)



# Control Strategies for Open-End Winding Drives Operating in the Flux-Weakening Region

Paul Sandulescu<sup>1</sup>, Fabien Meinguet<sup>1</sup>, Xavier Kestelyn<sup>1</sup>, Eric Semail<sup>1</sup>, Antoine Bruyère<sup>2</sup>

**Abstract**—This paper presents and compares control strategies for three-phase open-end winding drives operating in the flux-weakening region. A six-leg inverter with a single dc-link is associated with the machine in order to use a single energy source. With this topology, the zero-sequence circuit has to be considered since the zero-sequence current can circulate in the windings. Therefore, conventional over-modulation strategies are not appropriate when the machine enters in the flux-weakening region. A few solutions dealing with the zero-sequence circuit have been proposed in literature. They use a modified space vector modulation or a conventional modulation with additional voltage limitations. The paper describes the aforementioned strategies and then a new strategy is proposed. This new strategy takes into account the magnitudes and phase angles of the voltage harmonic components. This yields better voltage utilization in the  $dq$  frame. Furthermore, inverter saturation is avoided in the zero-sequence frame and therefore zero-sequence current control is maintained. Three methods are implemented on a test bed composed of a three-phase permanent-magnet synchronous machine, a six-leg inverter and a hybrid DSP/FPGA controller. Experimental results are presented and compared for all strategies. A performance analysis is conducted as regards the region of operation and the machine parameters.

**Index Terms**—AC machines, Current control, Fault-tolerance, Field weakening, Harmonic components, H-bridge, Modulation strategies, Open-end windings, Permanent magnet machines, Space vector pulse width modulation, Variable speed drives

## I. INTRODUCTION

OPEN-END winding machines have been used in various drive applications. Early works focused generally on fault-tolerant capability [1], [2]. Further investigations have shown other advantages, such as a reduced complexity compared with multi-level inverter drives [3], increased power for the same ratings of switching components compared with the conventional star-connected topology [4], the possibility to integrate a charger functionality without any additional component for electric vehicles [5], [6], a method to boost the supply voltage [7] and a topology for supplying the machine

with two isolated sources that can exchange energy between them [8].

Several converter topologies have been suggested to be associated with three-phase open-end winding machines [9].

Independent full-bridge converters (with different sources, DSPs, sensors and so forth) are the most appropriate as regards fault-tolerance, but are only cost-effective for critical applications in which failures have dramatic effects.

Topologies with two three-leg inverters are alternative solutions to reduce the cost of the system. In case there are two isolated sources and thus separate DC-links, the zero-sequence current cannot circulate. This is an advantage for the healthy operation as current ripple and Joule losses are reduced. Fault-tolerant capability of this topology is discussed in [10], showing that some fault conditions can be handled by creating an artificial neutral point with the faulty inverter, at the expense of a phase-voltage drop of half the initial value.

On the other hand, a topology with a single dc-link has the advantage to reduce the drive cost, while offering a good fault-tolerant capability since the machine can be operated with two active phases. In the latter case, the sum of the healthy phase currents has to be different from zero in order to eliminate torque ripple [11], [12]. This can be obtained through a zero-sequence path. With this topology, a control strategy for handling the zero-sequence current in healthy operation is required as well.

Problems associated with the zero-sequence current are generally due to a low zero-sequence inductance and thus a low time constant, yielding high-frequency current ripple in case a two-level modulation strategy is used. In [13], a modified space-vector pulse-width modulation (SV-PWM) strategy is presented, in which the common mode voltage is eliminated. This allows an elimination of the high-frequency zero-sequence current as well, as all selected vectors have an instantaneous zero-sequence voltage equal to zero. However, the zero-sequence circuit is then short-circuited and triplen harmonic current components can circulate. The magnitude of the zero-sequence current depends on the machine parameters, i.e. the zero-sequence emf, inductance and stator resistance. In some cases, this current can be large and therefore other modulation techniques, apart from two-level PWM techniques, need to be used as conventional three-level PWMs for instance [14], [15], [16].

In case a conventional modulation technique is used, vectors with a zero-sequence voltage different from zero can be applied. Compared with star-connected machines, there is an

<sup>1</sup> Paul Sandulescu, Fabien Meinguet, Xavier Kestelyn, and Eric Semail are with Arts et Métiers - ParisTech, L2EP, 8, Boulevard Louis XIV, 59046 Lille, FRANCE phone:+330320621561

<sup>2</sup> Antoine Bruyère is with Valeo Powertrain, 14, avenue des Béguines, 95800 Cergy Saint-Christophe, France

Corresponding author e-mail: ERIC.SEMAIL@ensam.eu

important difference regarding inverter saturation. When six-step or quasi-six-steps strategies are applied to star-connected machines, fifth- and seventh-harmonic components affect the voltages and currents [17], [18], [19], [20]. Considering a six-leg inverter, triplen harmonics, i.e. those associated with the zero-sequence component, have to be considered as well.

In case of inverter saturation, the magnitude of the third-harmonic voltage component can be larger than those of the fifth and seventh harmonics. This, combined with a low zero-sequence inductance, can have dramatic effects on the phase currents. Consequently, inverter saturation has to be avoided.

In [22], inverter saturation is avoided by reducing the maximum fundamental voltage available in the  $dq$  reference frame.

In this paper, strategies proposed in [13], [14], [21] and [22] are first recalled. These strategies will be referred to as Zero-space vector modulation (Z-SVM) and voltage-limited PWM (VL-PWM). An analysis of experimental results highlighting the properties of both strategies is conducted.

Next, it is shown that the strategy proposed in [22] is based on a worst case analysis and can be substantially improved. Through the analysis of a waveform composed of fundamental- and third-harmonic components, the importance of the relative phase and magnitudes of both harmonics is highlighted. A new voltage limit is then calculated, yielding better voltage source inverter utilization. An implementation of this strategy is also proposed, which will be referred to as zero-sequence harmonic detection (ZSHD) in what follows.

For each strategy, a calculation of the voltage limits is given and a detailed control scheme is proposed. It has to be noted that a conventional flux-weakening strategy is applied, which can be found in a vast body of literature [23], [24], [25], [26], [27], [28].

Finally, a comparison of the three strategies is performed and hints for the selection of the appropriate strategy as a function of the machine parameters are given.

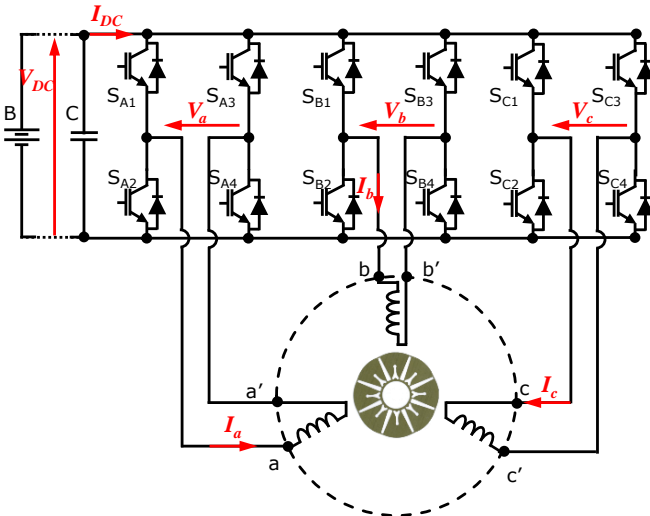


Fig. 1. Drive topology with a single energy source, a six-leg inverter and a three-phase PMSM with open-end windings.

## II. DRIVE MODEL

The drive topology under study is shown in Fig. 1. The PMSM and inverter models are described in the following sections.

### A. Open-end Winding PMSM Modeling

Neglecting the effects of saliency and magnetic saturation, the model of PMSMs is given by:

$$\begin{bmatrix} V_a \\ V_b \\ V_c \end{bmatrix} = R_s \begin{bmatrix} I_a \\ I_b \\ I_c \end{bmatrix} + [L_{abc}] \frac{d}{dt} \begin{bmatrix} I_a \\ I_b \\ I_c \end{bmatrix} + \begin{bmatrix} E_a \\ E_b \\ E_c \end{bmatrix} \quad (1)$$

where  $V_{abc}$  are the voltages at the machine terminals,  $R_s$  the stator resistance,  $I_{abc}$  the phase currents,  $[L_{abc}]$  the inductance matrix and  $E_{abc}$  the electromotive force (emf) due to the permanent magnets. Neglecting emf harmonic components beyond the third harmonic, the emf is described by  $E_{abc} =$

$$\begin{bmatrix} E_a \\ E_b \\ E_c \end{bmatrix} = \Omega \hat{K}_t \begin{bmatrix} \sin(\theta_e) + k_{fem3} \sin(3\theta_e + \pi) \\ \sin(\theta_e - \frac{2\pi}{3}) + k_{fem3} \sin(3(\theta_e - \frac{2\pi}{3}) + \pi) \\ \sin(\theta_e - \frac{4\pi}{3}) + k_{fem3} \sin(3(\theta_e - \frac{4\pi}{3}) + \pi) \end{bmatrix}$$

where  $\Omega$  is the mechanical angular velocity,  $\hat{K}_t$  is the emf constant and  $k_{fem3}$  is the amount of third harmonic component with respect to the fundamental harmonic.

The electrical equations of open-end windings PMSMs expressed in the rotor reference frame are given by (2) after

$$\text{successively applying Concordia } [C] = \sqrt{\frac{2}{3}} \begin{bmatrix} \frac{1}{\sqrt{2}} & \frac{1}{\sqrt{2}} & \frac{1}{\sqrt{2}} \\ 1 & -\frac{1}{2} & -\frac{1}{2} \\ 0 & \frac{\sqrt{3}}{2} & -\frac{\sqrt{3}}{2} \end{bmatrix}$$

$$\text{and rotational } [R] = \begin{bmatrix} 1 & 0 & 0 \\ 0 & \cos(\theta_e) & \sin(\theta_e) \\ 0 & -\sin(\theta_e) & \cos(\theta_e) \end{bmatrix}$$

transformations:

$$\begin{bmatrix} V_0 \\ V_d \\ V_q \end{bmatrix} = R_s \begin{bmatrix} I_0 \\ I_d \\ I_q \end{bmatrix} + \begin{bmatrix} L_0 & 0 & 0 \\ 0 & L_d & 0 \\ 0 & 0 & L_q \end{bmatrix} \frac{d}{dt} \begin{bmatrix} I_0 \\ I_d \\ I_q \end{bmatrix} + \omega_e \begin{bmatrix} e(3\theta_e) \\ -L_q I_q \\ L_d I_d + \psi_{M,1} \end{bmatrix} \quad (2)$$

In what follows, it will be considered that :

$$\omega_e \begin{bmatrix} e(3\theta_e) \\ -L_q I_q \\ L_d I_d + \psi_{M,1} \end{bmatrix} = \begin{bmatrix} E_0 \\ E_d \\ E_q \end{bmatrix} \quad (3)$$

where  $L_0$  is the zero-sequence inductance,  $L_d$  and  $L_q$  the  $d$ - and  $q$ -axis inductances respectively,  $\omega_e$  the electrical angular velocity and  $\theta_e$  the electrical position. The zero-sequence emf  $E_0$  is composed of a third harmonic component and is thus a function of  $3\theta_e$  that can be expressed as  $E_0 = \omega_e e(3\theta_e)$  with  $e(3\theta_e) = \sqrt{3} \frac{\hat{K}_t}{N_{pp}} k_{fem3} \sin(3\theta_e)$ , where  $N_{pp}$  is the number of pole pairs. Due to the Concordia transformation, a square root coefficient is present, as it is shown later on in Table III. The

terms  $E_d$  and  $E_q$  depend on the value of the fundamental flux linkage due to the permanent magnets  $\psi_{M,1}$ , the coupling terms and possibly other harmonic components which are not multiple of three (neglected in this approach).

Under the assumption of negligible saliency and neglecting emf harmonic components beyond the third harmonic, the electromagnetic torque is given by:

$$T_{em} = N_{pp}[\psi_{M,1}I_q + e(3\theta_e)I_0] \quad (4)$$

The parameters of the PMSM under study are given in Table I. It is worth noticing that  $L_0 = L_d/24$  and  $|e(3\theta_e)|$  refers to the peak value of  $e(3\theta_e)$  in the zero-sequence frame. A weak value of  $L_0$  in comparison with  $L_d$  value is quite common for 3-phase electrical machine with strong mutual couplings. In this case,  $L_0$  is close to the leakage inductance. The high ratio will induce constraint on the control.

TABLE I : PMSM parameters

Parameter	Value
$R_s$	0.475Ω
$L_d = L_q$	8.4mH
$L_0$	0.35mH
$\psi_{M,1}$	0.314 V s/rad
$ e(3\theta_e) $	0.010 V s/rad
$N_{pp}$	4
$ I_{abc,max} $	20.4A

### B. Six-leg Inverter Modeling

The converter output voltage with respect to the  $x$ -phase ( $x \in \{a, b, c\}$ ) is equal to:

$$V_x = \begin{cases} +V_{DC} & \text{if } (S_{x1} \text{ AND } S_{x4}) \\ 0 & \text{if } (S_{x1} \text{ AND } S_{x3}) \\ 0 & \text{if } (S_{x2} \text{ AND } S_{x4}) \\ -V_{DC} & \text{if } (S_{x2} \text{ AND } S_{x3}) \end{cases} \quad (5)$$

that leads to  $2^6=64$  possible combinations of switching states.

From the 64 switching combinations, considering the voltage vector that may be applied to the three independent phases of the machine ( $V_x$ ), only 27 different voltage vectors appear. As in the case of the three-phase VSI, where 8 vectors are generated by the different switching combinations and only 7 appears as different for a three-phase star-coupled machine windings, in the case of the open-end winding machine, from the 64 vectors generated by the inverter only 27 appears as different for the machine, the rest being redundant.

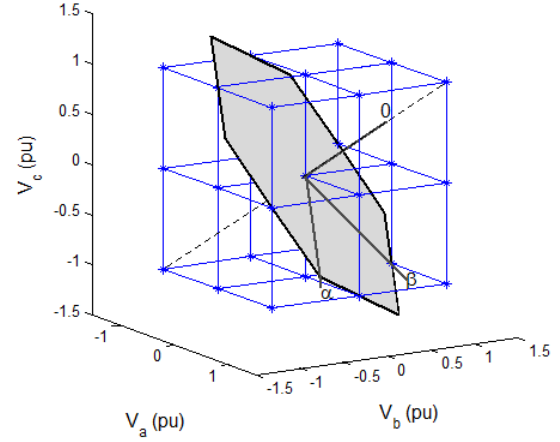


Fig. 2. Voltage vectors in the  $abc$  space (normalized by  $V_{DC}$ ). The grey hexagon shows the projection of the cube in the  $\alpha\beta$  space, whereas one diagonal of the cube (black dashed line) is oriented along the zero-sequence axis.

A 3D-representation of the VSI is possible by considering the three phase voltages of the machine. In the  $abc$  reference frame the 27 voltage vectors are shown in Fig. 2 (values are normalized by  $V_{DC}$ ). The voltage vectors form a cube in the  $abc$  reference frame.

The grey hexagon in Fig. 2 corresponds to the projection of the cube in the  $\alpha\beta$  reference frame, obtained by applying the Concordia transformation. In addition to the  $\alpha\beta$  plane, similar to the case where a three-phase star-coupled machine is used, a zero-sequence component is also present. The zero-sequence component is projected over the zero-sequence axis that is oriented along a diagonal of the cube.

In what follows, values are presented in  $pu$ , with the voltage values normalized by  $V_{DC}$  and currents values by  $|I_{abc,max}|$ . Due to the Concordia transformation, coefficients appear when expressed in  $pu$ . These coefficients are given in Table II and Table III for currents and voltages respectively.

TABLE II : Per unit values of the coefficient in the  $abc$  and  $\alpha\beta$  reference frames (currents)

$I_a(t)$	$ I_{abc,pu} $	$ I_{\alpha\beta,pu} $	$ I_{0,pu} $
$ I_{abc,max}  \sin \omega_e t$	1	$\sqrt{3/2}=1.2247$	0
$ I_{abc,max}  \sin 3\omega_e t$	1	0	$\sqrt{3}=1.7321$

TABLE III : Per unit values of the coefficient in the  $abc$  and  $\alpha\beta$  reference frames (voltages)

$V_a(t)$	$ V_{abc,pu} $	$ V_{\alpha\beta,pu} $	$ V_{0,pu} $
$V_{DC} \sin \omega_e t$	1	$\sqrt{3/2}=1.2247$	0
$V_{DC} \sin 3\omega_e t$	1	0	$\sqrt{3}=1.7321$

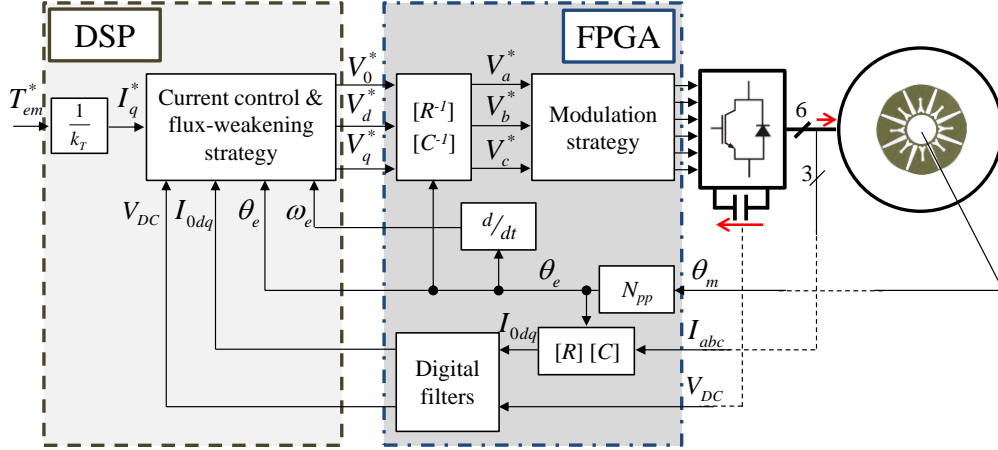


Fig. 3. General block diagram of the control scheme

### III. CONTROL STRATEGIES

The general control scheme is shown in Fig. 3 and different versions of the DSP block will be examined in this paper (Fig. 5; Fig. 9; Fig. 14). The current reference  $I_q^*$  is obtained from the torque reference  $T_{em}^*$  by inverting (4). Assuming a negligible contribution of the zero-sequence component to the torque generation,  $I_q^*$  is given by:

$$I_q^* = \frac{T_{em}^*}{k_t} \quad (6)$$

where  $k_t$  is the torque constant of the electric machine only due to the first harmonic component of the emf.

Control and flux-weakening algorithms are handled within the DSP, while data acquisition, modulation strategy, Concordia and rotational transformations, filtering and signal conditioning are deported on the FPGA.

Three control strategies are presented in the following sections, focusing on the current control. An identical integrator-based solution is implemented for all flux-weakening strategies [24]. However, an important difference

consists in the voltage limits which are different for each strategy. Modulation strategies are briefly addressed as well.

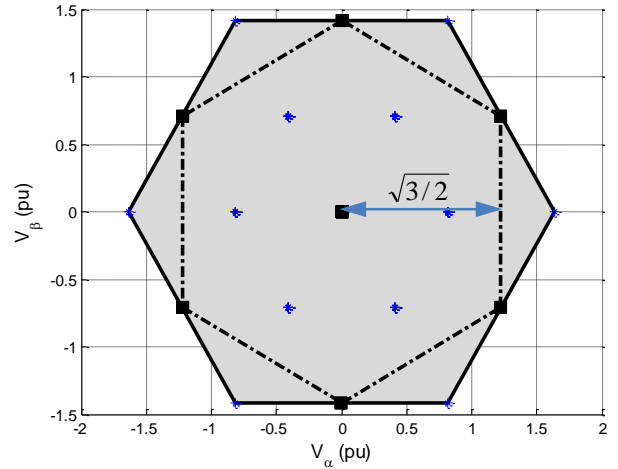


Fig. 4. Projections of the voltage vectors on to the  $a\beta$  plane. The outer hexagon is the projection of the cube, whereas the inner hexagon (black dashdot line) is the surface delimited by vectors having a zero-sequence voltage component equal to zero.

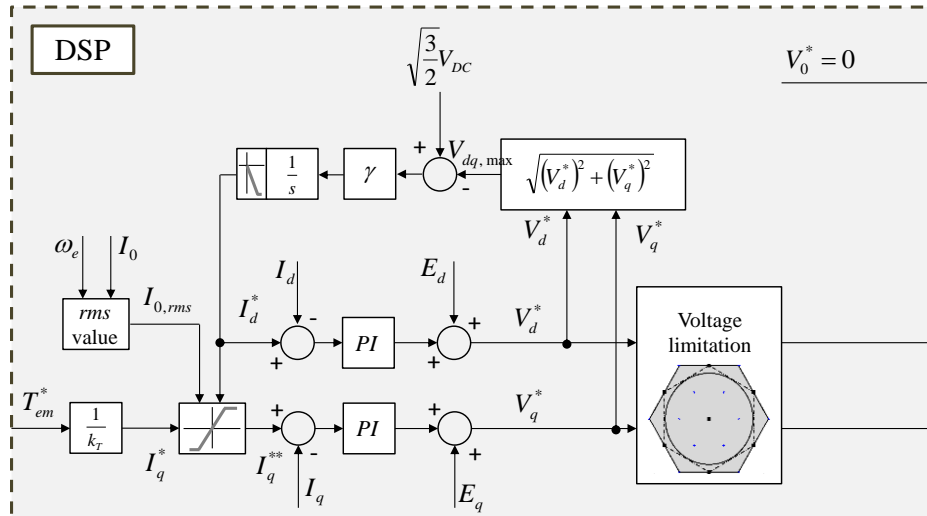


Fig. 5. Control block diagram for the strategy based on voltage vectors having a zero-sequence component equal to zero (Z-SVM).

### A. Zero Space-Vector Modulation (Z-SVM)

Basics of the Zero-SVM are presented in [13], whereas implementation details for FPGA are discussed in [14]. The strategy consists in selecting vectors having an instantaneous zero-sequence voltage component equal to zero. Among these vectors, six form a hexagon in the  $\alpha\beta$  plane defined by  $V_0 = 0$ , as depicted in Fig. 4, dashed hexagon. Using these six vectors and zero vectors, a conventional SVM can be implemented. The  $abc$  ( $\alpha\beta$ ) voltage limit is equal to  $1 pu$  ( $\sqrt{3/2} pu$ ) in case of linear modulation, whereas this value can be increased in case six-step or quasi-six step strategies are used. In what follows, only linear modulations are presented for the sake of comparison between the strategies.

With this strategy,  $V_0$  is equal to zero and therefore, from (2):

$$I_0 = \frac{-E_0}{R_s + sL_0} \quad (7)$$

Hence, the zero-sequence current only depends on the machine parameters.

The control block diagram associated with this strategy is given in Fig. 5.

First, the  $q$ -axis current reference is saturated according to a maximum Joule losses criterion:

$$I_q^{**} = \sqrt{(I_q^*)^2 - (I_d^*)^2 - I_{0,rms}^2} \quad (8)$$

where  $I_q^{**}$  denotes the saturated  $q$ -axis reference,  $I_d^*$  is the output of the flux-weakening controller, which is chosen as an integrator with gain  $\gamma$ . The difference between the voltage limitation  $\sqrt{1.5}V_{DC}$  and the magnitude of the  $dq$  voltage references ( $V_d^*$  and  $V_q^*$ ) is integrated and yields  $I_d^*$ . The integrator output is limited between 0 and  $-I_{dq,max}$ . The voltage references are also saturated according to the voltage limitation:

$$|V_{dq}^{**}| \leq \sqrt{\frac{3}{2}} V_{DC} \quad (9)$$

with  $|V_{dq}^{**}|$  the modulus of the saturated voltage references (phase is kept constant).

Experimental results of the proposed strategy are shown in Fig. 6. The test has been conducted with  $\omega_m = 215 \text{ rad s}^{-1}$ ,  $V_{DC} = 200\text{V}$ ,  $I_q^* = 25\text{A}$  and a PWM frequency equal to  $10\text{kHz}$ . For this operating point, the machine is operated in the flux-weakening region and the currents are such that  $I_q^{**} = 18\text{A}$ ,  $I_d^* = -16\text{A}$  and  $I_{0,rms} = 7.68\text{A}$ . A verification of the current limitation is obtained through the following calculation:

$$\sqrt{I_q^{**2} + I_d^{*2} + I_{0,rms}^2} = \sqrt{\frac{3}{2}} |I_{abc,max}| = 25\text{A} \quad (10)$$

The plot shows one phase current (CH1) and the sum of the phase currents (CH2), which is related to the zero-sequence current through the Concordia transformation as follows:

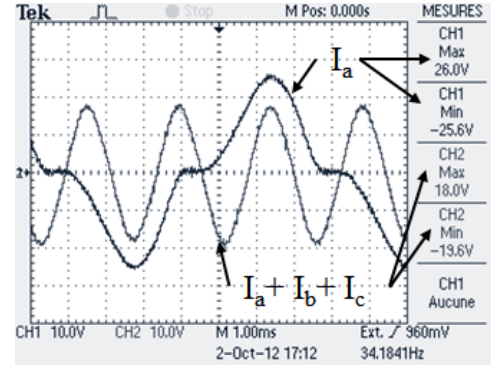


Fig. 6. Waveforms of one phase current (CH1) and of the sum of the phase currents (CH2) for the Zero Space Vector Modulation strategy (Z-SVM). The conversion factor is 1V equals 1A.

$$I_0 = \frac{1}{\sqrt{3}} (I_a + I_b + I_c) \quad (11)$$

Fig. 6 shows three interesting properties of this control strategy:

1. the high-frequency current ripple is very low. This is due to the elimination of the instantaneous zero-sequence voltage component and a large value of the  $dq$ -axis inductance for this machine.
2. the RMS value of the zero-sequence current can be high, (depends on the machine parameters). In this case, the ratio of Joule losses compared with the fundamental component is equal to 10%.
3. the peak value of the phase current can be very large (depends on the relative phase between the third-harmonic and the fundamental components). In this case, the peak amplitude increases of about 31%.

Consequently, although the high-frequency zero-sequence current is eliminated, the third-harmonic component is still responsible for additional Joule losses (both inverter and machine losses), IGBT and heat sink oversizing, magnetic saturation and increase of iron losses in the machine. Furthermore, torque ripple due to the zero-sequence current can appear as well.

Additional experimental results are presented in Fig. 7. The test shows the machine starting at time  $t=0\text{s}$  and with a  $100\text{rad s}^{-2}$  acceleration maintained throughout 2.5 seconds. The torque reference is such that  $I_q^* = 25\text{A}$ .

Fig. 7(a) shows the  $0dq$  currents. Initially, all currents are close to their reference, i.e.  $I_q = 25\text{A}$ ,  $I_d = 0\text{A}$  and  $I_0$  is low. The  $dq$  currents have a sixth-harmonic component due to additional induced voltages. The zero-sequence current is primarily composed of a third-harmonic component.

The drive enters the flux-weakening region at time  $t=1.7\text{s}$ . As the machine was operated at rated torque, the current limitation immediately applies. From  $t=1.7\text{s}$  until  $t=2.5\text{s}$ , the  $d$ -axis current becomes negative in order to maintain the voltage reference under the voltage limitation. It is interesting to observe that the zero-sequence current increases in the flux weakening region. This is due to magnetic saturation that decreases the value of the zero-sequence inductance.

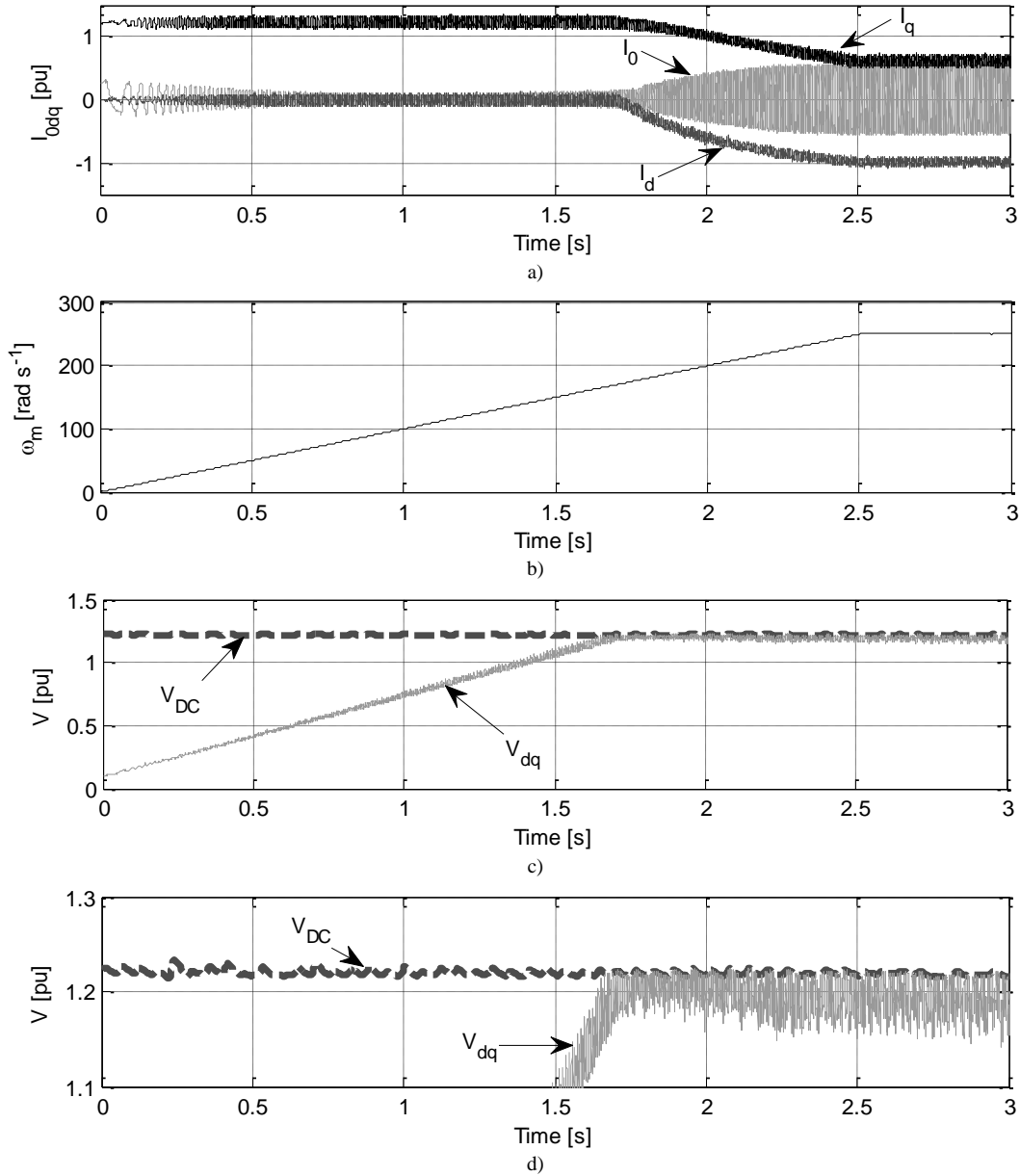


Fig. 7. Experimental results of the flux-weakening strategy with the zero Space Vector Modulation (Z-SVM): a) Synchronous currents; b) Mechanical speed; c) DC-link voltage and  $dq$  voltage references; d) DC-link voltage and  $dq$  voltage references (zoom).

Saturated voltage references are shown in Fig. 7(c) and (d), which indicate that the magnitude of the  $dq$  voltage references are equal to  $\sqrt{1.5} pu$  in the flux-weakening region.

#### B. Conventional Modulation with an Additional Voltage Limitation (VL-PWM)

In the previous section, it was shown that it might be interesting to select voltage vectors which have an instantaneous zero-sequence component different from zero. The objective is to eliminate the third-harmonic current component. Obviously, it is not possible to eliminate both the third-harmonic current component (due to the machine emf) and the high-frequency current ripple (due to the inverter voltage). In this section, effects of a zero-sequence voltage

reference different from zero are evaluated. The modulation strategy that is used is referred to as “three-level simple modulation” in [14].

In case any of the 27 voltage vectors can be used, the voltage references have to be kept inside the cube (see Fig. 2). New voltage limitations have to be defined in this case, as illustrated in Fig. 8.

Considering a voltage vector  $\vec{V}_s$  with a given zero-sequence component  $V_0$ , the closest surface delimiting the cube is shown in Fig. 8. The projection of  $\vec{V}_s$  gives the maximum component available along the  $\alpha$  axis. For an absolute value of the zero-sequence component ranging from 0 to  $\sqrt{3} pu$ , the voltage limit is a straight line passing through points A and B.



The equation of the straight line passing through these points A and B is given by:

$$AB : V_\alpha = \sqrt{\frac{3}{2}} - \frac{V_0}{\sqrt{2}} \quad [pu] \quad (12)$$

Eq. (12) is consistent with the voltage limitation proposed in [19].

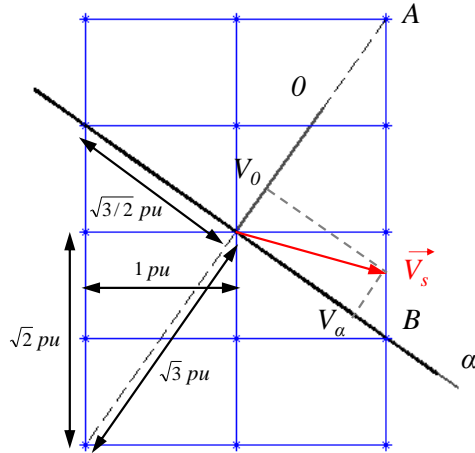


Fig. 8. Projection of a voltage vector  $\vec{V}_s$  in the  $\alpha\theta$  plane.

Under the assumption of a single harmonic component in the zero-sequence circuit, the maximum value of the  $dq$  voltage references can be expressed as:

$$V_{dq,max} = \sqrt{\frac{3}{2}} - V_{0,RMS}^* \quad [pu] \quad 13)$$

Hence, a zero-sequence voltage component different from zero affects the maximum voltage available in the  $dq$  reference frame.

The corresponding control block diagram is shown in Fig. 9. The zero-sequence current is now controlled, in a similar way compared with the  $dq$  currents, i.e. through a PI controller and emf compensation (feed-forward). The zero-sequence voltage reference  $V_0^*$  passes through a RMS calculation block, whose output is used to calculate the voltage limitation (13).

The  $q$ -axis current reference is still saturated according to (8).

Obviously,  $V_{dq,max}$  is now used to saturate the voltage reference. Hence, (9) becomes:

$$|V_{dq}^{**}| \leq \sqrt{\frac{3}{2}} V_{DC} - V_{0,RMS}^* \quad (14)$$

Experimental results of the proposed strategy are shown in Fig. 10. The test has been conducted in the same conditions as for Fig. 6, i.e. with  $\omega_m=215 \text{ rad s}^{-1}$ ,  $V_{DC}=200\text{V}$ ,  $I_q^*=25\text{A}$  and a PWM frequency equal to 10kHz.

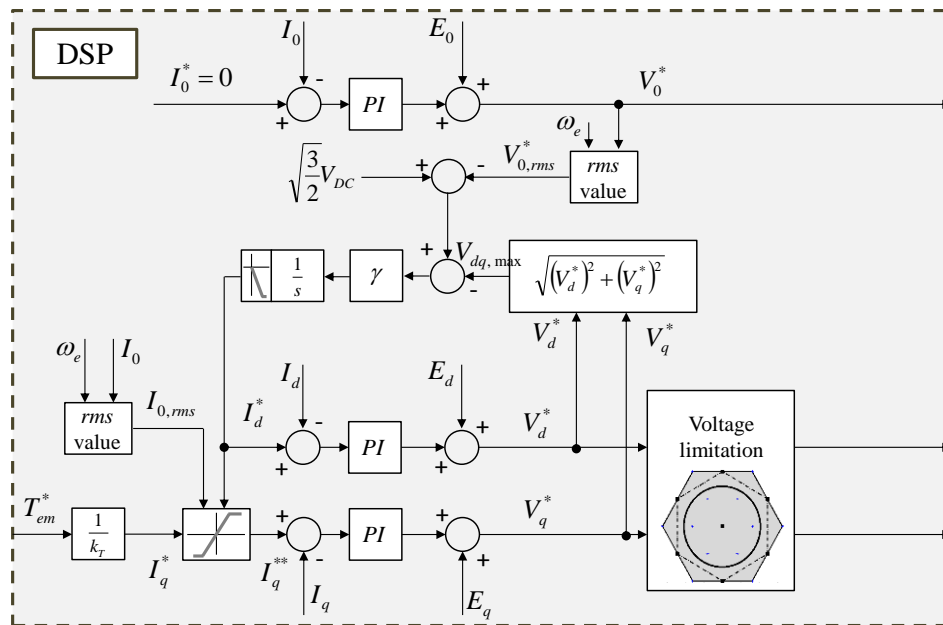


Fig. 9. Control block diagram for the strategy with a conventional modulation and additional voltage limitations accounting for the zero-sequence voltage (VL-PWM)

For this operating point, the machine is operated in the flux weakening region and the currents are such that  $I_q^{**}=17.4\text{A}$ ,  $I_d^*=-17.9\text{A}$  and  $I_{0,rms}=1.5\text{A}$ .

The properties of this strategy are:

1. the high-frequency current ripple is larger than the ripple of the Z-SVM, but acceptable for the machine under study.

2. the value of the zero-sequence current can be high, (depends on the machine parameters), but primarily because of the high-frequency current ripple. The increase in Joule losses due to the third-harmonic component is negligible.
3. the peak value of the phase current can be large (depends on the zero-sequence inductance). In this case, the peak amplitude increases of about 24%.



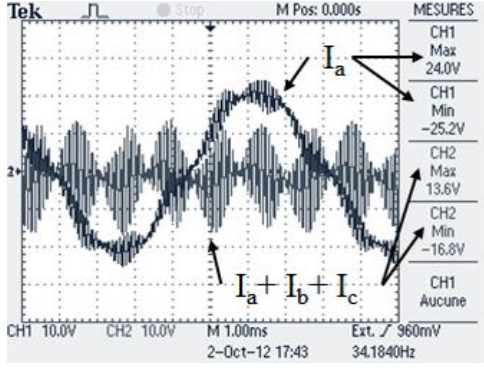


Fig. 10. Waveforms of one phase current (CH1) and of the sum of the phase currents (CH2) for the conventional modulation and an additional voltage limitation (VL-PWM). The conversion factor is 1V equals 1A.

Additional experimental results are presented in Fig. 11. The test shows the machine starting at time  $t=0$ s and with a  $100\text{rad s}^{-2}$  acceleration maintained throughout 2.5 seconds. The torque reference is such that  $I_q^*=25\text{A}$ .

The drive enters the flux-weakening region at time  $t=1.7$ s. A main difference compared with the Z-SVM is the control over the zero-sequence current, which is close to zero in the flux-weakening region.

The other major difference is the voltage limitation (see Fig. 11(c) and (d)). As the zero-sequence voltage reference is different from zero, the maximum  $dq$  voltage decreases. At  $\omega_m=250\text{ rad s}^{-1}$  the maximum voltage is about 5% lower. This has an effect on the flux-weakening algorithm which requires a larger  $d$ -axis current (absolute value) in order to fulfill the

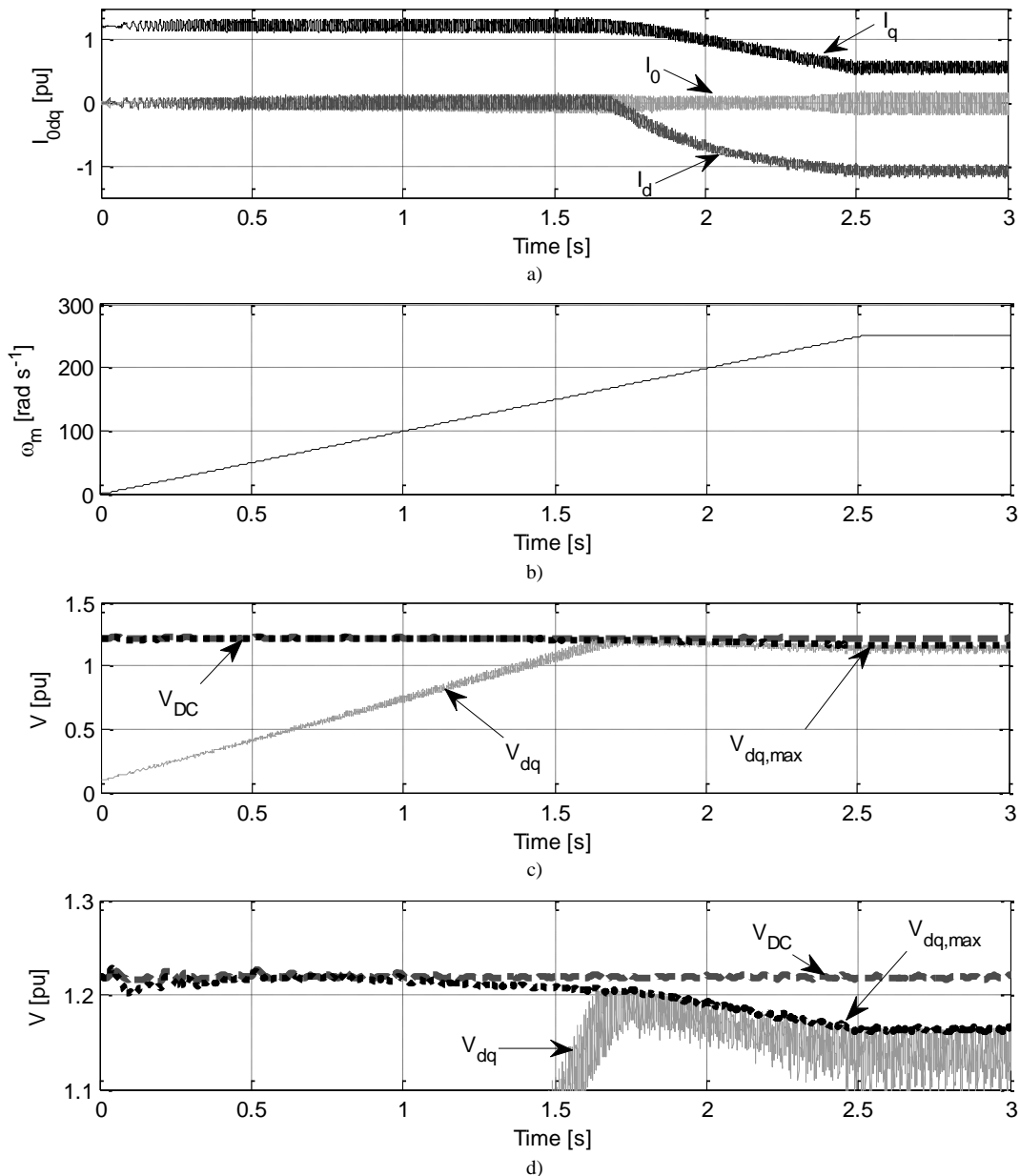


Fig. 11. Experimental results of the flux-weakening strategy with a conventional modulation and an additional voltage limitation (VL-PWM): a) Synchronous currents; b) Mechanical speed; c) DC-link voltage and  $dq$  voltage references; d) DC-link voltage and  $dq$  voltage references (zoom).

voltage constraint (14).

### C. New Strategy Accounting for the Phase and Amplitude of the Zero-Sequence Harmonic Component (ZSHD)

In the previous section, it was shown that voltage vectors that have a zero-sequence component different from zero have reduced  $\alpha\beta$  components. Actually, Fig. 8 shows the projection of a voltage vector which yields a worst case analysis. The derived equation (12) is obtained by considering that both maxima are obtained simultaneously, i.e. that the maximum values of  $V_0$  and of  $V_a$  occur at the same time.

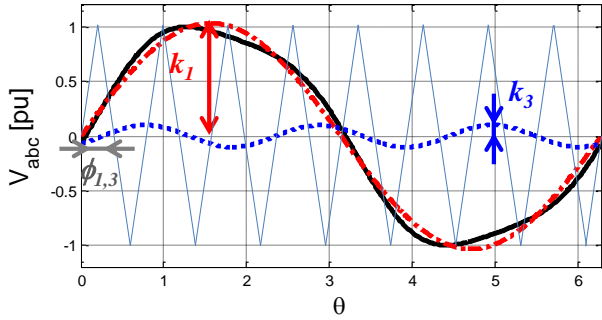


Fig. 12. Waveform composed of fundamental and third-harmonic components (solid black line), its fundamental-harmonic component (dashdotted red line) and its third harmonic component (dotted blue line):  $k_1=1.035$ ,  $k_3=0.1$  and  $\phi_{1,3}=-\pi/4$ .

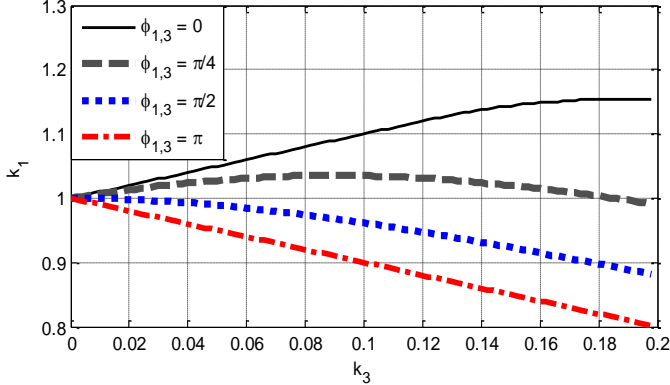


Fig. 13. Maximum value of the fundamental component  $k_1$  as a function of the amplitude  $k_3$  for different relative phases  $\phi_{1,3}$ .

A further analysis is presented in this section. The  $abc$  reference frame gives a good representation of the problem to be solved as the voltage limit can be simply expressed as:

$$|V_{abc,pu}| \leq 1 \text{ [pu]} \quad (15)$$

Assuming only voltage fundamental- and third-harmonic components, the voltage of phase  $a$  can be expressed as follows:

$$V_a = k_1 \sin \omega t + k_3 \sin(3\omega t + \phi_{1,3}) \quad (16)$$

where  $k_1$ ,  $k_3$  are the magnitudes of the fundamental and third-harmonic components respectively, whereas  $\phi_{1,3}$  is the phase displacement between these harmonics, the fundamental component being the absolute phase reference. Fig. 12

illustrates a waveform composed of fundamental and third-harmonic components. The maximum value of  $V_a$  is equal to one. For the chosen set of parameters, i.e.  $k_1 = 1.035$ ,  $k_3 = 0.1$  and  $\phi_{1,3} = -\pi/4$ , it is shown that the fundamental value is larger than the DC-link voltage.

As mentioned in the introduction section, an objective of the control strategy is to prevent inverter saturation, which can lead to large zero-sequence currents as the zero-sequence inductance can be very low. Therefore, the zero-sequence voltage calculated by the controller has to be applied to the machine and the problem consists thus in calculating the maximum fundamental or  $dq$  voltage limit.

Therefore, the problem is reduced to determining  $k_1$  that fulfills (16) when  $V_a = 1$  and for given  $k_3$  and  $\phi_{1,3}$ . Although the problem seems simple, the solution given by symbolic math software is rather complex and is not appropriate for a real-time implementation. For the proposed implementation, the calculation is performed offline and a lookup table with two inputs ( $k_3$  and  $\phi_{1,3}$ ) and one output ( $k_1$ ) is generated. This relation is shown in Fig. 13, which depicts the maximum fundamental voltage  $k_1$  as a function of the third-harmonic component  $k_3$  and for various relative phases  $\phi_{1,3}$ . The figure highlights that the relative phase has an important contribution. For example, in case  $k_3=0.18$ , relative phases equal to  $\phi_{1,3}=0$  and  $\phi_{1,3}=\pi$  yield  $k_1=1.15$  and  $k_1=0.82$  respectively, i.e. a difference of about 40%. It is interesting to note that the worst case of section III.B. corresponds to the case  $\phi_{1,3}=\pi$  (straight line).

Fig. 14 shows the control block diagram associated with the proposed control strategy. The major difference compared with the scheme of Fig. 9 is the phase and envelope detector which allows the optimal fundamental voltage to be calculated. This block is further described in Fig. 15.

The saturated voltage references  $V_d^{**}$  and  $V_q^{**}$  are used to calculate the phase angle of the fundamental component, which is multiplied by three to be consistent with the phase angle of the third-harmonic component.

The processing is a little more complex as regards the zero-sequence component. A quadrature-signal generator (QSG) which generates a  $90^\circ$ -lagging signal is first applied to the zero-sequence voltage reference [12], [29]. Two  $90^\circ$ -shifted signals with pulsation equal to  $3\omega_e$  are thus obtained, i.e.  $V_{0,\alpha}^*$  and  $V_{0,\beta}^*$ . These signals are then transformed into constant signals by applying a rotation matrix with a rotation angle equal to  $3\theta_e$ . Finally, the constant values  $V_{0,d}^*$  and  $V_{0,q}^*$  are used to calculate the phase angle of the third-harmonic component  $\phi_3$  and its magnitude  $k_3$ . The difference between both phase angles  $\phi_{1,3}$  is then calculated.

From  $\phi_{1,3}$  and  $k_3$ , the lookup table allows  $k_1$  to be found. This coefficient multiplies the DC-link voltage to determine the maximum  $dq$  fundamental voltage  $V_{dq,max}$ . An additional lowpass filter (not represented in the figure) is required to avoid an algebraic loop involving the saturated voltage outputs  $V_d^{**}$  and  $V_q^{**}$ .

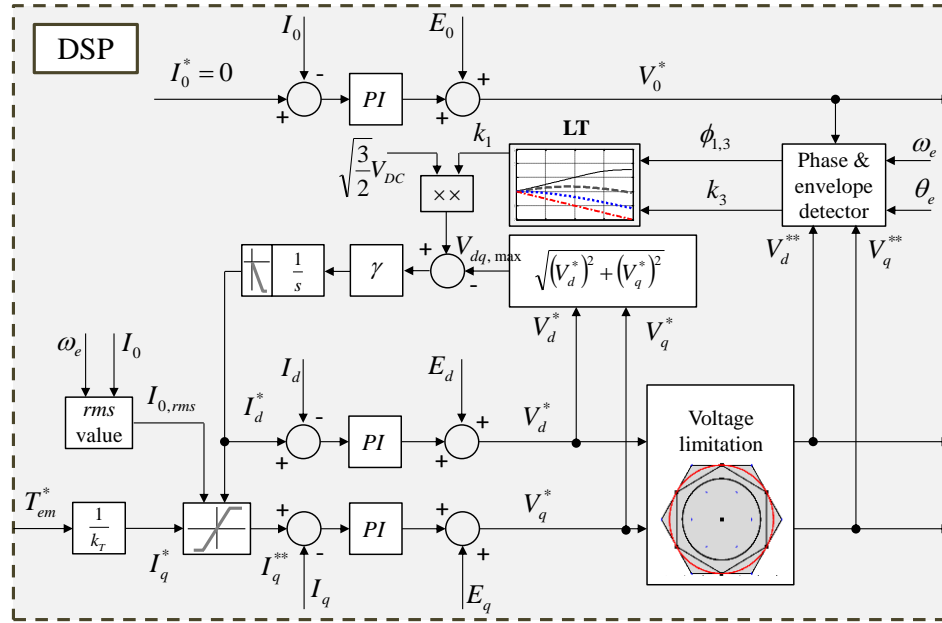


Fig. 14. Control block diagram for the strategy accounting for the amplitude and phase of the zero-sequence voltage (ZSHD).

Experimental results of the proposed strategy are shown in Fig. 16. The test has been conducted in the same conditions as for Fig. 6 and Fig. 10, i.e. with  $\omega_m=215 \text{ rad s}^{-1}$ ,  $V_{DC}=200\text{V}$ ,  $I_q^*=25\text{A}$  and a PWM frequency equal to 10 kHz. For this operating point, the machine is operated in the flux weakening region and the currents are such that  $I_q^{**}=19.4\text{A}$ ,  $I_d^*=-15.9\text{A}$  and  $I_{0,rms}=1.5\text{A}$ .

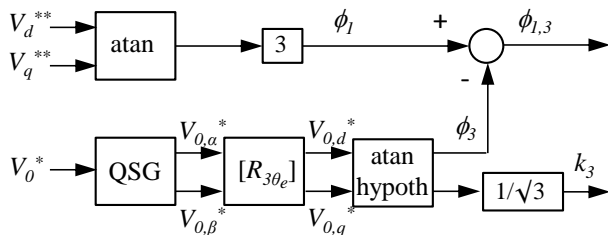


Fig. 15. Zero-sequence relative phase and envelope detection.

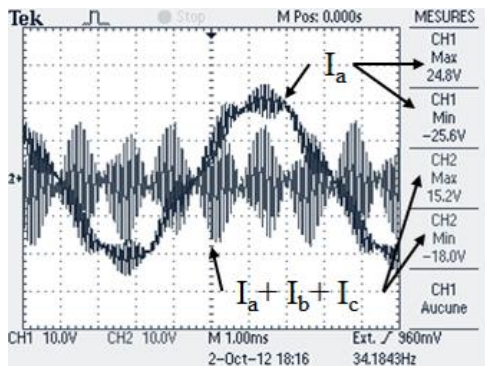


Fig. 16. Waveforms of one phase current (CH1) and of the sum of the phase currents (CH2) for a conventional modulation and the strategy accounting for the phase and amplitude of the third harmonic component. The conversion factor is 1V equals 1A.

The waveform is similar to the waveform shown in Fig. 10. However, a difference is noticeable regarding the values of the  $q$ - and  $d$ -axis currents (see section IV for a comparison between the strategies).

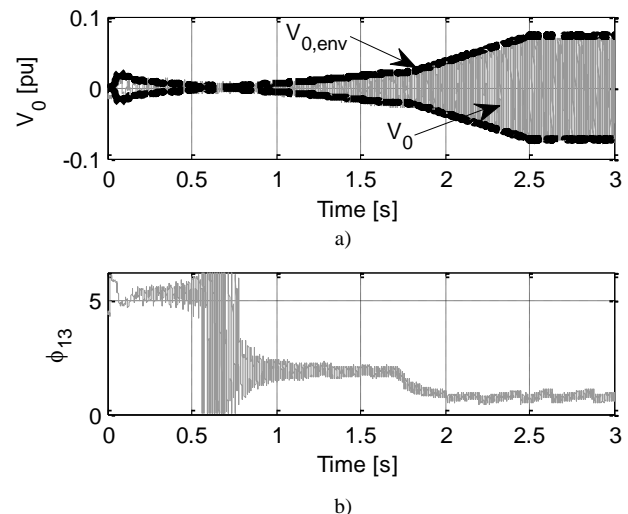


Fig. 17. Experimental results of the zero-sequence detection for a speed ramp at maximum torque: a) Zero-sequence voltage and its envelope signal; b) Phase difference between the fundamental and the third-harmonic.

Fig. 17 illustrates the zero-sequence harmonic detection for a test where the machine starts rotating at time  $t=0$ s with a  $100 \text{ rad/s}^2$  acceleration lasting for 2.5 seconds (see speed profile in Fig. 18(b)). The torque reference is such that  $I_q^* = 25\text{A}$ . Fig. 17 is associated with Fig. 18 showing the  $0dq$  currents, speed profile and  $dq$  voltage references.

Fig. 17 (a) shows the zero-sequence voltage reference and its envelope obtained through the scheme of Fig. 15. Initially, the zero-sequence emf is low. However, the PI controller injects a zero-sequence voltage different from zero. The origin

of this voltage is the compensation of the non-linearity due to the inverter voltage drops and dead-time. The same phenomenon has been identified in simulations.

The zero-sequence emf becomes the largest component when the speed increases. The value is approximately equal to  $0.02 \text{ pu}$  when the machine enters the flux-weakening region at time  $t=1.7\text{s}$ . It is worth noticing that the zero-sequence voltage still increases in the flux-weakening region (up to  $7.5\%$ ), while the  $dq$ -components are maintained approximately constant. Therefore, even machines with a low zero-sequence emf can present a significant amount of zero-sequence voltage in the flux-weakening region, for instance machines with large

$dq$  inductances designed to be operated in a large constant-power region.

Fig. 17(b) shows the relative phase between the fundamental and third harmonic components. Initially constant, the phase shifts from  $180^\circ$  when the zero-sequence voltage crosses zero at time  $t=0.7\text{s}$ . The relative phase is approximately constant when the speed increases at rated torque. The phase changes however significantly when the machine enters the flux weakening region. The phase is approximately equal to  $2 \text{ rad}$  ( $115^\circ$ ) at  $\omega_m=170 \text{ rad s}^{-1}$  and ends equal to  $0.8 \text{ rad}$  ( $45^\circ$ ) at  $\omega_m=250 \text{ rad s}^{-1}$ , i.e. a difference of  $70^\circ$ , which is primarily due to a change of the  $dq$ -axis voltage references.

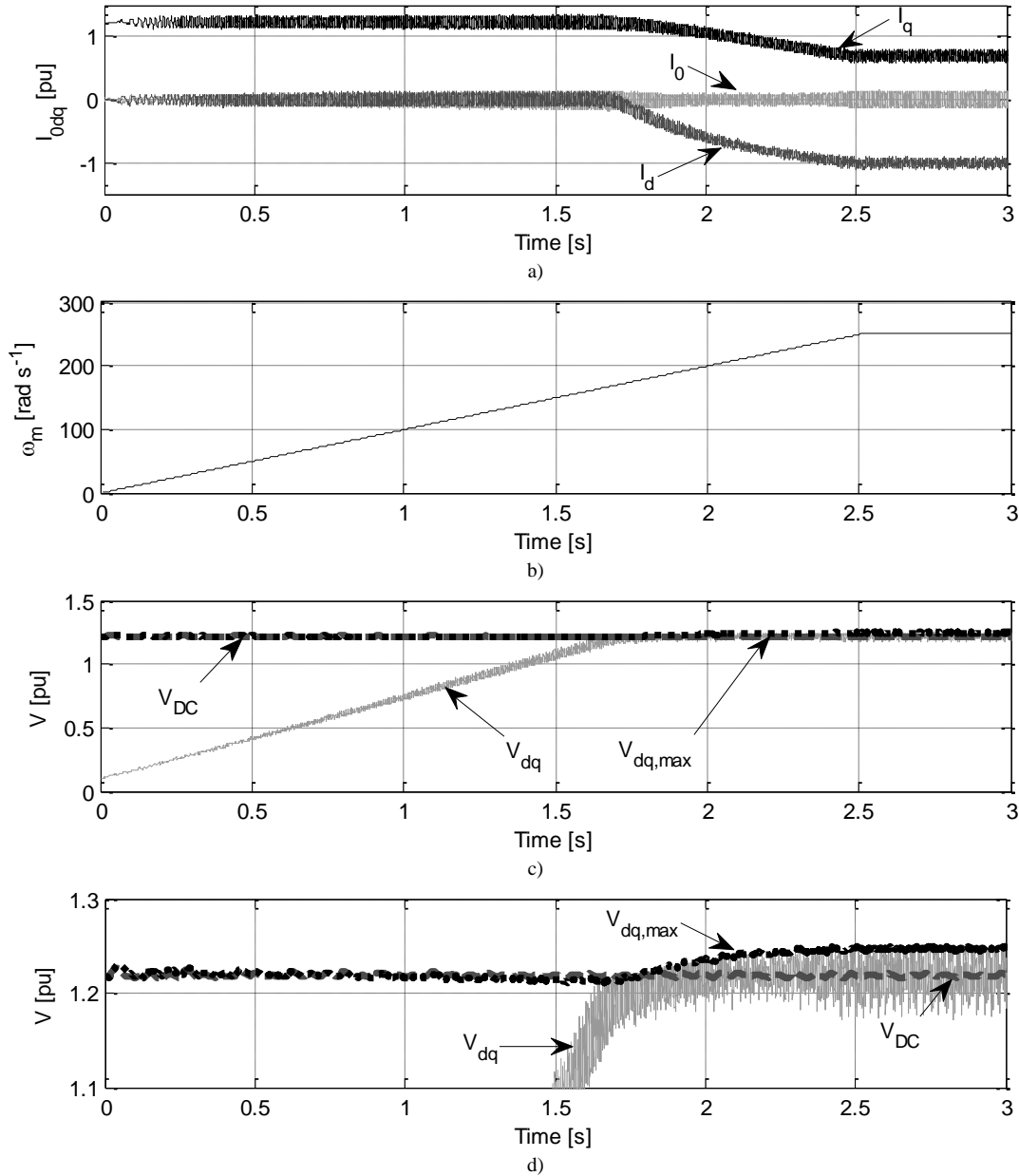


Fig. 18. Experimental results of the flux-weakening strategy with a conventional modulation and the proposed strategy (zero-sequence harmonic detection, ZSHD): a) Synchronous currents; b) Mechanical speed; c) DC-link voltage and  $dq$  voltage references; d) DC-link voltage and  $dq$  voltage references (zoom).

Regarding the voltage limitations, Fig. 18(d) shows that  $V_{dq,max}$  is larger than 1.22 pu, i.e. that the maximum fundamental component is larger than the DC-link voltage. The experimental value obtained with  $\omega_m=250$  rad s<sup>-1</sup> is 2.4% larger than the DC-link voltage. This value is equivalent to the coefficient  $k_1$  that can be found in Fig. 13 with  $k_3 = V_{0,env}/\sqrt{3} = \frac{0.075}{1.71} = 0.043$  and  $\phi_{1,3} = \frac{\pi}{4} = 0.8$ .

Compared with Fig. 11(d), there is thus a maximum voltage increase of 2.4% instead of a decrease of 5%.

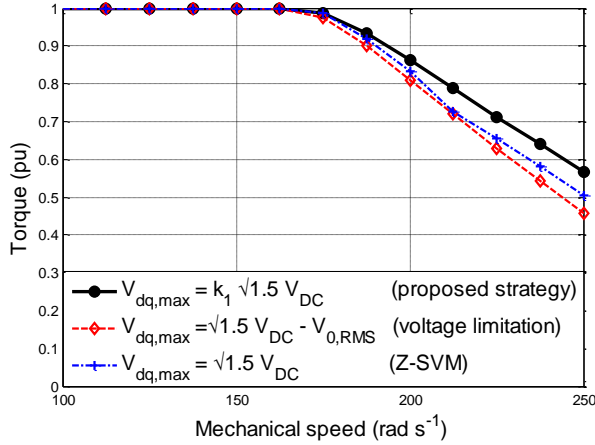


Fig. 19. Comparison of the torque vs speed curve for the strategies under study.

#### IV. COMPARISON OF THE CONTROL STRATEGIES

Fig. 19 compares the three strategies as regards the torque versus speed characteristic for the machine under study. It shows that the proposed strategy (ZSHD) has superior performances in terms of maximum torque and thus efficiency in the flux-weakening region, followed by the Z-SVM and the voltage-limited PWM (VL-PWM).

The performance of the ZSHD strategy compared with the voltage-limited strategy is simple to be analyzed. In Fig. 20 a) and b), the  $abc$  voltage references are shown for both strategies, corresponding to the tests presented in Fig. 11 and Fig. 18 respectively. The voltage references for the voltage limited strategy are lower than the maximum values equal to  $\pm 1$ . This is due to the strategy which considered a worst case for the voltage limitation. This problem is addressed in the proposed implementation by taking into account the relative phase and magnitude of the zero-sequence component, yielding a better use of the DC-link voltage (see Fig. 20 b)).

Compared with the Z-SVM, the superiority of the proposed ZSHD strategy is due to two factors. First, the zero-sequence voltage allows an increase of the fundamental component. Although this is a well-known property for star-connected machines, the constraint on the zero-sequence current is such that the gain depends on the machine parameters, primarily the zero-sequence emf but also the  $dq$  inductances, which influence the phase of the voltage fundamental component. Next, the zero-sequence current can be significant using the Z-SVM strategy. As the Joule losses are accounted in the saturation of the  $q$ -axis current reference, the maximum torque is reduced when the machine is operated at maximum Joule

losses. These losses depend on the machine parameters as well, as the zero-sequence short-circuit current depends approximately on the ratio  $|e(3\theta_e)|/L_0$ .

The electric machine parameters have thus an important impact on the different strategies. This is summarized in Table IV, which can be used as a qualitative tool to select the appropriate strategy as a function of the machine parameters. Multiple strategies can also be embedded in the controller with an appropriate switching from one strategy to another in function of the operating conditions.

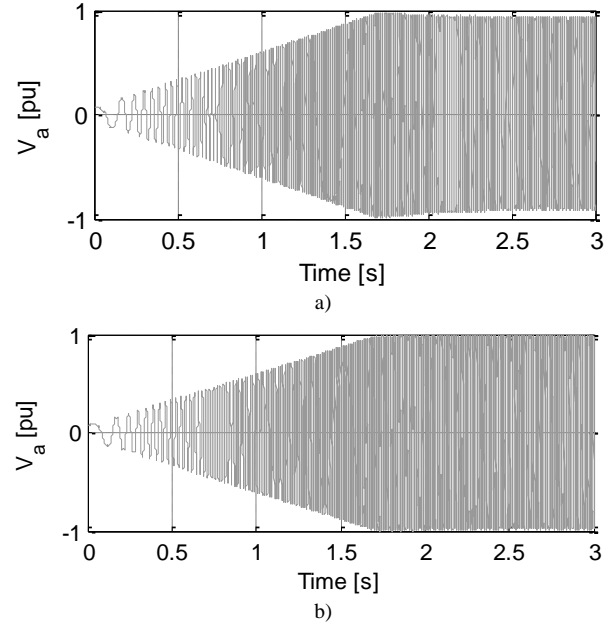


Fig. 20. Comparison of the voltage references for two strategies: a) Voltage-limited strategy (VL-PWM); b) Zero-sequence harmonic detection strategy (ZSHD).

#### V. CONCLUSION

This paper has presented three different control strategies for open-end winding drives operated in the flux-weakening region. The topology under study has the particularity to have one single energy source; therefore a zero-sequence path exists and this has to be accounted for in the control loops.

The first method consists in modifying the modulation strategy to eliminate zero-sequence high-frequency current ripple. However, triplen harmonics appear and it is shown that their effect can be worse than the effect of high-frequency current ripple.

Consequently, a second strategy is presented. A conventional modulation is used, and triplen harmonics are eliminated by the control loop. The worst case analysis is presented to show that the maximum  $dq$  voltage has to be reduced in function of the zero-sequence voltage. This simple analysis gives good results but proved not to be optimal.

Finally, a third strategy is proposed. Although similar to the second, this strategy takes into account the phase and magnitude of the third-harmonic component to determine the maximum  $dq$  voltage. This yields a better utilization of the DC-link voltage while preventing inverter saturation of the zero-sequence circuit.

TABLE IV : Qualitative evaluation of the three strategies under study.

	Z-SVM	VL-PWM	ZSHD	Comments
$L_0 \ll$	++	-	-	High-frequency zero-sequence current ripple is eliminated with Z-SVM and can be problematic for conventional modulation strategies (peak currents, losses,...)
$ e(3\theta_e) /L_0 \gg$	--	++	++	Low-frequency zero-sequence current ripple is eliminated with VL-PWM and ZSHD and can be problematic with Z-SVM (peak currents, losses, torque ripple,...)
$ e(3\theta_e)  \gg$	-/+	--	--/++	The benefits/drawbacks for the Z-SVM depend on $L_0$ . For the VL-PWM, large values of $ e(3\theta_e) $ will reduce the maximum $dq$ voltage in the flux weakening region, while large values can reduce or increase the maximum $dq$ voltage for ZSHD (depend on parameters and operating conditions).
Common mode voltage elimination	++	--	--	This is an inherent property of the Z-SVM that other methods cannot achieve.

Finally, a comparison showed that the proposed strategy has superior performances for the machine under study. However, the performances are strongly dependent on the machine parameters, as discussed throughout the paper.

The problems arising when an open-end winding is associated with a six-leg inverter have been presented and it is shown that several solutions are available. Modifications of the modulation strategy are possible, but an appropriate machine design is also mandatory to obtain better performances.

Future research will be directed to extend the proposed flux-weakening strategy to multiphase machines. For these machines, the determination of the voltage and current limits for each harmonic component is yet to solve.

## VI. ACKNOWLEDGMENTS

The authors would like to thank FUI for the support and funding of the SOFRACI project.

## REFERENCES

- [1] T.J. Jahns, "Improved Reliability in Solid-State AC Drives by Means of Multiple Independent Phase Drive Units," *IEEE Transactions on Industry Applications*, vol. IA-16, no.3, pp.321-331, May 1980
- [2] B.C. Mecrow, A.G. Jack, J.A. Haylock, and J. Coles, "Fault-tolerant permanent magnet machine drives," *IEE Proceedings on Electric Power Applications*, vol.143, no.6, pp.437-442, Nov 1996
- [3] K.A. Corzine, S.D. Sudhoff, and C.A. Whitcomb, "Performance characteristics of a cascaded two-level converter," *IEEE Transactions on Energy Conversion*, vol.14, no.3, pp.433-439, Sep 1999
- [4] Welchko, B.A.; Nagashima, J.M.;, "The influence of topology selection on the design of EV/HEV propulsion systems," *IEEE Power Electronics Letters*, vol.1, no.2, pp.36-40, June 2003
- [5] L. De-Sousa, B. Bouchez, "Combined Electric Device for Powering and Charging," International Patent WO 2010/057892 A1, 2010
- [6] L. De Sousa, B. Silvestre, B. Bouchez, "A combined multiphase electric drive and fast battery charger for Electric Vehicles," *IEEE Vehicle Power and Propulsion Conference (IEEE-VPPC 2010)*, pp. 1-6, 1-3 September 2010.
- [7] J. Ewanchuk, J. Salmon, and C. Chapelsky, "A Method for Supply Voltage Boosting in an Open-Ended Induction Machine Using a Dual Inverter System With a Floating Capacitor Bridge," *IEEE Transactions on Power Electronics*, vol.28, no.3, pp.1348-1357, March 2013

- [8] B.A. Welchko, J.M. Nagashima, G.S. Smith, S. Chakrabarti, M. Perisic, and G. John, "Double ended inverter system with an impedance source inverter subsystem", US Patent US 7,956,569 B2, June 2011
- [9] B.A. Welchko, T.M. Jahns, and T.A. Lipo, "Short-circuit fault mitigation methods for interior PM synchronous machine drives using six-leg inverters," *Power Electronics Specialists Conference, 2004. PESC 04. 2004 IEEE 35th Annual*, vol.3, pp. 2133- 2139, 20-25 June 2004
- [10] Y. Wang, T.A. Lipo, and D. Pan, "Robust operation of double-output AC machine drive," *2011 IEEE 8th International Conference on Power Electronics and ECCE Asia (ICPE & ECCE)*, pp.140-144, May 30 2011-June 3 2011
- [11] S. Bolognani, M. Zordan, and M. Zigliotto, "Experimental fault-tolerant control of a PMSM drive," *IEEE Transactions on Industrial Electronics*, vol.47, no.5, pp.1134-1141, Oct 2000
- [12] F. Meinguet, X. Kestelyn, E. Semail, and J. Gyselinck, "Fault detection, isolation and control reconfiguration of three-phase PMSM drives," *2011 IEEE International Symposium on Industrial Electronics (ISIE)*, pp.2091-2096, 27-30 June 2011
- [13] M.R. Baiju, K.K. Mohapatra, R.S. Kanchan, and K. Gopakumar, "A dual two-level inverter scheme with common mode voltage elimination for an induction motor drive," *IEEE Transactions on Power Electronics*, vol.19, no.3, pp. 794- 805, May 2004
- [14] P. Sandulescu, L. Idkhajine, S. Cense, F. Colas, X. Kestelyn, E. Semail, and A. Bruyere, "FPGA Implementation of a General Space Vector Approach on a 6-Leg Voltage Source Inverter," *IECON 2011 - 37th Annual Conference on IEEE Industrial Electronics Society*, pp.3482-3487, 7-10 Nov. 2011
- [15] Pou, J.; Zaragoza, J.; Ceballos, S.; Saeedifard, M.; Boroyevich, D., "A Carrier-Based PWM Strategy With Zero-Sequence Voltage Injection for a Three-Level Neutral-Point-Clamped Converter," *IEEE Transactions on Power Electronics*, vol.27, no.2, pp.642,651, Feb. 2012
- [16] Dordevic, O.; Levi, E.; Jones, M., "A Vector Space Decomposition Based Space Vector PWM Algorithm for a Three-Level Seven-Phase Voltage Source Inverter," *IEEE Transactions on Power Electronics*, vol.28, no.2, pp.637,649, Feb. 2013
- [17] G. Griva, T.G. Habetler, F. Profumo, and M. Pastorelli, "Performance evaluation of a direct torque controlled drive in the continuous PWM-square wave transition region," *IEEE Transactions on Power Electronics*, vol.10, no.4, pp.464-471, Jul 1995
- [18] A.M. Hava, S.-K. Sul, R.J. Kerkman, and T.A. Lipo, "Dynamic overmodulation characteristics of triangle intersection PWM methods," *IEEE Transactions on Industry Applications*, vol.35, no.4, pp.896-907, Jul/Aug 1999
- [19] T.-S. Kwon; G.-Y. Choi, M.-S. Kwak, and S.-K. Sul, "Novel Flux-Weakening Control of an IPMSM for Quasi-Six-Step Operation," *IEEE Transactions on Industry Applications*, vol.44, no.6, pp.1722-1731, Nov.-Dec. 2008



- [20] Hesong Liu, Z.Q. Zhu, E. Mohamed, Yongling Fu, and Xiaoye Qi, "Flux-Weakening Control of Nonsalient Pole PMSM Having Large Winding Inductance, Accounting for Resistive Voltage Drop and Inverter Nonlinearities," *IEEE Transactions on Power Electronics*, vol.27, no.2, pp.942-952, Feb. 2012
- [21] Somasekhar, V.T.; Srinivas, S.; Kumar, K.K., "Effect of Zero-Vector Placement in a Dual-Inverter Fed Open-End Winding Induction Motor Drive With Alternate Sub-Hexagonal Center PWM Switching Scheme," *IEEE Transactions on Power Electronics*, vol.23, no.3, pp.1584,1591, May 2008
- [22] A.P. Sandulescu, F. Meinguet, X. Kestelyn, E. Semail and A. Bruyere, "Flux-weakening operation of open-winding drive integrating a cost-effective high-power charger", *IET Electrical Systems in Transportation*, vol.3, no.1, pp.10,21, March 2013
- [23] F. Briz, A. Diez, M.W. Degner, and R.D. Lorenz, "Current and flux regulation in field-weakening operation [of induction motors]," *IEEE Transactions on Industry Applications*, vol.37, no.1, pp.42-50, Jan/Feb 2001
- [24] L. Harnefors, K. Pietilainen, and L. Gertmar, "Torque-maximizing field-weakening control: design, analysis, and parameter selection," *IEEE Transactions on Industrial Electronics*, vol.48, no.1, pp.161-168, Feb 2001
- [25] T.-S. Kwon, S.-K. Sul, "Novel Antiwindup of a Current Regulator of a Surface-Mounted Permanent-Magnet Motor for Flux-Weakening Control," *IEEE Transactions on Industry Applications*, vol.42, no.5, pp.1293-1300, Sept.-Oct. 2006
- [26] M. Tursini, E. Chiricozzi, and R. Petrella, "Feedforward Flux-Weakening Control of Surface-Mounted Permanent-Magnet Synchronous Motors Accounting for Resistive Voltage Drop," *IEEE Transactions on Industrial Electronics*, vol.57, no.1, pp.440-448, Jan. 2010
- [27] S. Bolognani, S. Calligaro, R. Petrella, and F. Pogni, "Flux-weakening in IPM motor drives: Comparison of state-of-art algorithms and a novel proposal for controller design," *Proceedings of the 2011-14th European Conference on Power Electronics and Applications (EPE 2011)*, pp.1-11, Aug. 30 2011-Sept. 1 2011
- [28] S. Bolognani, S. Calligaro, and R. Petrella, "Optimal voltage feed-back flux-weakening control of IPMSM," *37th Annual Conference on IEEE Industrial Electronics Society IECON 2011*, pp.4170-4175, 7-10 Nov. 2011
- [29] P. Rodriguez, R. Teodorescu, I. Candela, A. V. Timbus, M. Liserre, and F. Blaabjerg, "New positive-sequence voltage detector for grid synchronization of power converters under faulty grid conditions," *37th IEEE Power Electronics Specialists Conference, 2006. PESC'06*. 2006, pp. 1-7, 18-22 June 2006.

## BIOGRAPHY



**Paul Sandulescu** (S'10) received the M.S. degree in electrical engineering from Politehnica University of Bucharest in 2009. He received the Ph.D. degree in electrical engineering from Arts et Métiers ParisTech, L2EP, Lille, France, in 2013. His research interests include multiphase machine drive system modeling, control and power electronics for automotive applications.



**Fabien Meinguet** (M'13) received the Master's degree in electrical engineering and the Ph.D. degree from the Université libre de Bruxelles, Brussels, Belgium, in 2007 and 2012, respectively. He is currently a Postdoc with Arts et Métiers ParisTech, Laboratory of Electrical Engineering and Power Electronics of Lille (L2EP), Lille, France. His main research interests are fault-tolerant drives, including design, control, and diagnosis.



**Xavier Kestelyn** (M'08) was born in Dunkerque, France, in 1971. He received the Ph.D. degree in electrical engineering from Lille University, France, in 2003.

He is currently an Associate Professor of electrical engineering at engineering school of Arts et Métiers ParisTech with the Laboratory of Electrical Engineering and Power electronics of Lille (L2EP), Lille, France. His research interests are in modeling and control of multi-machine systems such as multi-phase machines and over-actuated industrial robots.



**Eric Semail** (M'02) received the M.S. degree from Ecole Normale Supérieure, Paris, France, in 1986 and the Ph.D. degree, with specializations in tools and the method of polyphase electrical systems and generalization of the space vector theory, from Lille University, Lille, France, in 2000.

He is currently with the Centres d'Enseignement et de Recherche, Arts et Métiers ParisTech, Laboratory of Electrical Engineering and Power Electronics of Lille (L2EP), where he became an Associate Professor in 2001 and a full Professor in 2010. With L2EP, his fields of interest include the design, modeling, and control of multiphase drives (converters and ac drives). More generally, he studies multimachine and multiconverter systems. His application fields are automotive, marine, and offshore wind power.



**Antoine Bruyere** has been working with Valeo since 2005 on the topics of hybrid and electric automotive vehicles. In 2009, he received his Electrical Engineering PhD degree from Arts et Métiers ParisTech school (France). He became *Valeo-Expert* in 2012, in the fields of Motor Drives, System Engineering, Electrical Machines and Electromagnetism. Now, he works as System Team Leader for the Valeo GEN2 Inverter/Charger project. He is in charge of the numerical control software development management.